PCCP

Cite this: *Phys. Chem. Chem. Phys.*, 2012, **14**, 12919–12929

www.rsc.org/pccp

PAPER

A DFT study on photoinduced surface catalytic coupling reactions on nanostructured silver: selective formation of azobenzene derivatives from *para*-substituted nitrobenzene and aniline†

Liu-Bin Zhao, Yi-Fan Huang, Xiu-Min Liu, Jason R. Anema, De-Yin Wu,* Bin Ren and Zhong-Qun Tian

Received 10th May 2012, Accepted 30th July 2012
DOI: 10.1039/c2cp41502j

We propose that aromatic nitro and amine compounds undergo photochemical reductive and oxidative coupling, respectively, to specifically produce azobenzene derivatives which exhibit characteristic Raman signals related to the azo group. A photoinduced charge transfer model is presented to explain the transformations observed in *para*-substituted $ArNO_2$ and $ArNH_2$ on nanostructured silver due to the surface plasmon resonance effect. Theoretical calculations show that the initial reaction takes place through excitation of an electron from the filled level of silver to the lowest unoccupied molecular orbital (LUMO) of an adsorbed $ArNO_2$ molecule, and from the highest occupied molecular orbital (HOMO) of an adsorbed $ArNH_2$ molecule to the unoccupied level of silver, during irradiation with visible light. The *para*-substituted $ArNO_2^{-\bullet}$ and $ArNH_2^{+\bullet}$ surface species react further to produce the azobenzene derivatives. Our results may provide a new strategy for the syntheses of aromatic azo dyes from aromatic nitro and amine compounds based on the use of nanostructured silver as a catalyst.

Introduction

Although heterogeneous photocatalysts are almost exclusively semiconductors, it has been demonstrated recently that plasmonic noble metal nanostructures also show significant promise.[1] The photochemistry of small molecules on noble metal and other nanostructures has become a subject of growing interest because of the unique optical, electrical and chemical properties that these surfaces can offer.[2,3] A comparison of photochemistry on band-gap semiconductors and plasmonic noble metal nanostructures is given in Scheme 1. In the case of band-gap semiconductors, absorption of photons with energy larger than the band gap generates electron–hole pairs (electrons in the conduction band or CB, and holes in the valence band or VB). These electrons and holes may then separate from each other and diffuse at the interface between the semiconductor and its environment. There they may drive chemical transformations. In the case of plasmonic noble metal nanostructures, photons of visible light are resonantly absorbed and they excite localized surface plasmons (LSPs) or surface plasmon polaritons (SPPs). Surface plasmons are collective oscillations in the density of negatively-charged valence electrons against the restoring force of their positively-charged nuclei.[4] It has been shown recently that plasmonic metal nanostructures can exhibit high photocatalytic activities.[5–9]

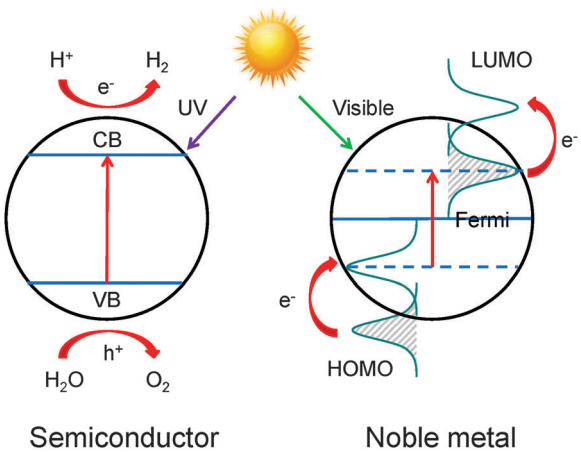

Scheme 1 A comparison of photochemistry on band-gap semiconductors and plasmonic noble metal nanostructures.

State Key Laboratory of Physical Chemistry of Solid Surfaces, and College of Chemistry and Chemical Engineering, Xiamen University, Xiamen, 361005, Fujian, China. E-mail: dywu@xmu.edu.cn; Fax: +86-592-2186979; Tel: +86-592-2189023

† Electronic supplementary information (ESI) available: Testing the reliability of theoretical methods, Raman spectra calculated with other clusters, normal mode analysis of important molecules on the basis of potential energy distribution, and simulated pre-resonance Raman spectra for considering the excitation wavelength effect on adsorbed molecules interacting with silver clusters. See DOI: 10.1039/c2cp41502j

Direct observation of surface-enhanced photochemical reactions have indeed been reported,[10–15] and a theoretical model for enhanced photochemistry on noble metal nanostructures has been proposed by Nitzan and Brus.[11] They suggested two enhancement mechanisms. One arises from greatly increased optical electric field strength on these surfaces. The enhanced photochemistry is due to enhanced absorption in this case. The other arises from accumulated heat in the surface plasmon substrate during irradiation.[16]

Surface-enhanced Raman spectroscopy (SERS) is a powerful *in situ* technique for probing the transient surface species and studying reaction mechanisms. Among aromatic nitro compounds, the electrochemical and photochemical reduction of *p*-nitrothiophenol (PNTP) and *p*-nitrobenzoic acid (PNBA) has been investigated using SERS.[17–23] During cathode polarization or laser irradiation, most of the original peaks decrease in intensity and a set of new peaks appear. The explanation for these spectral changes has been debated, however. Some authors attribute the new peaks to amines as reduction products, since they are similar to the SERS features of corresponding aromatic amine species on nanostructured silver.[20,22,24] Others attribute the new peaks to azobenzene species.[17–19,23] Sun *et al.* concluded that the product could be either aniline species or azo compound or both.[18] To the best of our knowledge, Roth *et al.* were the first to propose a reductive coupling reaction to form *p*,*p*′-azodibenzoic acid (ADBA) during irradiation with high power laser light.[17] These authors also found that *p*-aminobenzoic acid (PABA) on silver reacts very quickly to form ADBA when exposed to atmospheric moisture and laser light.[25]

Aromatic amine compounds on silver surfaces also display very interesting SERS signals. SERS from *p*-aminothiophenol (PATP) on silver is significantly different from its ordinary Raman spectra in methanol solution and the solid state.[24–27] A series of experiments have shown that the SERS spectrum of PATP is strongly dependent on laser wavelength,[28,29] irradiation power[30,31] and the pH of solution.[26,32–34] The unusually intense peaks were initially explained by charge transfer between PATP and silver which causes selective enhancement of the signal from modes which are non-totally symmetric.[24] Recently, our theoretical calculations have shown that PATP molecules adsorbed on rough noble metal surfaces and noble metal nanoparticles undergo a surface catalytic coupling reaction to selectively produce *p*,*p*′-dimercaptoazobenzene (DMAB).[35,36] It is believed that DMAB is responsible for the unusual SERS spectra observed. Surface mass spectrometry measurements and SERS measurements on synthesized DMAB support the proposed chemical transformation of PATP to DMAB on silver.[31]

Although the photoinduced surface catalytic coupling reaction is also supported from other studied groups, some studies still interpreted the unusually intense Raman peaks from the charge transfer mechanism.[37,38] More recently, we reported the detailed analysis of surface Raman spectra of PATP itself adsorbed on silver, gold, and copper surfaces. Our results show that for adsorbed PATP molecules no fundamental frequency match well with experimentally observed frequencies and the charge transfer direction is from molecule to metal, opposite to the experimental observation.[39]

Although the formation of azobenzene species during SERS measurement of aromatic nitro and amine compounds has been proposed, the reaction mechanism is still unclear. In this study, the reaction mechanism and pathway of photoinduced surface catalytic coupling reactions of aromatic nitro and amine compounds on silver are investigated by density functional theory (DFT) methods. Our calculated results indicate that a number of *para*-substituted $ArNO_2$ and $ArNH_2$ adsorbed on silver surfaces undergo a photocatalytic coupling reaction to form azobenzene derivatives. We further extend our theoretical studies to the reaction mechanisms. We compare our own simulated Raman spectra of reactants, intermediates and products with experimentally obtained Raman spectra in the literature. A photoinduced charge transfer model based on time-dependent density functional theory (TD-DFT) is presented to explain the selectivity of the photoinduced surface catalytic reduction of $ArNO_2$ and oxidation of $ArNH_2$ on silver to aromatic azo compounds.

Computational details

Density functional calculations were carried out with the generalized gradient approximation (GGA) for the exchange–correlation functionals PW91PW91[40] and BP86,[41,42] and the hybrid exchange–correlation functional B3LYP.[43,44] The basis sets for the C, N, O, S and H atoms of the investigated molecules were 6-311+G(d, p), which includes a polarization function for all five kinds of atoms and a diffuse function for C, N, O and S atoms.[45,46] For all metal atoms, the valence electrons and the inner shell electrons were described by the basis set LANL2DZ and the corresponding relativistic effective core potentials, respectively.[47,48] Full geometry optimizations and analytic frequency calculations were carried out using the Gaussian 09 package.[49] To test the reliability of the theoretical methods, the molecular structures and vibrational spectra of nitrobenzene, aniline and azobenzene were calculated using different exchange–correlation functionals and compared with experimental data (see Section 1 in the ESI†). We found that the B3LYP method is good for describing N=O and the PW91PW91 method is good for describing N=N. Both B3LYP and PW91PW91 methods gave well description of aniline. So the vibrational analysis of $ArNO_2$ and $ArNH_2$ was performed by B3LYP while azobenzene derivatives were calculated by PW91PW91.

The metallic cluster model was used to extract the adsorption structure and to simulate the surface Raman spectra of *para*-substituted $ArNO_2$ and $ArNH_2$, as well as their reaction intermediates, on silver. Thiophenol derivatives adsorb onto the metal surfaces through the sulfur atom after the cleavage of the S–H bond. The thiol H atom of adsorbed thiophenol is removed in our calculation, as discussed in previous studies.[24,50] The Ag_{13} cluster was chosen to allow PNTP and PATP to adsorb vertically at hollow sites through their thiol groups. Benzoic acid derivatives adsorb on metal surfaces as benzoate salt (unprotonated form).[17,51] We adopt benzoic acid dissociatively adsorbed in the bridging bidentate geometry on the silver surface. The Ag_9^+ cluster was chosen to provide suitable bonding sites for the carboxylate groups of PNBA and PABA. Simulations with other silver clusters (Ag_n^{δ}, $n = 5$ and 7; $\delta = 0, +1$) give similar results (see Fig. S2 and S3, ESI†). This can

be understood by the strong localization bonding between adsorbates and silver clusters.

Absolute Raman intensities were calculated on top of the differential Raman scattering cross sections (DRSCs) as in our previous work.[35] In this case, the Raman scattering intensity was calculated using

$$I_{\mathrm{Raman}} = \frac{(2\pi)^4}{45}\frac{h}{8\pi^2 c\omega_i}\frac{(\omega_0-\omega_i)^4}{1-\exp(-hc\omega_i/k_{\mathrm{B}}T)}S_i$$

where

$$S_i = 45\left(\frac{\mathrm{d}\alpha}{\mathrm{d}Q_i}\right)^2 + 7\left(\frac{\mathrm{d}\gamma}{\mathrm{d}Q_i}\right)^2$$

is the Raman scattering factor (in Å^4 per amu) that can be calculated using Gaussian 09. S_i is calculated at the equilibrium geometry and it is only an expression of derivatives of the static isotropic (α) and anisotropic (γ) polarizabilities with respect to the given normal coordinate. Here the ω_0 and ω_i denote the frequency of the incident light and the vibrational frequency of the ith mode. To allow a direct comparison with experimentally obtained SERS data, the simulated Raman spectra were presented in terms of a Lorentzian expansion with a line width of 10 cm^{-1} and an excitation wavelength of 632.8 nm.

Electronic excitation was examined through the time-dependent DFT (TD-DFT) approach TD-B3LYP, which is efficient and offers an orbital picture for a physical understanding of the excitation process.[52] The TD-DFT results were used to predict CT directions in molecule–metal complexes. The photoinduced electron transfer processes can be visualized from analysis of the molecular orbitals involved in the CT excitations (photoinduced reduction is associated with metal-to-molecule CT and photoinduced oxidation is associated with molecule-to-metal CT).

Results

Surface Raman spectra of PNTP and PATP

The electrochemical and photochemical reductions of PNTP have been experimentally studied extensively using SERS.[20,23,53–55] Disappearance of the peak at 1346 cm^{-1} is generally found to coincide with the appearance of new bands at 1143, 1392 and 1436 cm^{-1}. In previous studies, these spectral changes were said to be from a nitro-to-amine reduction forming PATP.[20,23,53–55] Fig. 1 presents simulated SERS spectra of PNTP, PATP and DMAB on silver surfaces. The Raman spectrum of PNTP on silver is dominated by three strong bands at 1066, 1331 and 1582 cm^{-1}. They can be assigned to the C–S stretching mode ν(C–S), the –NO$_2$ symmetric stretching mode ν_s(NO$_2$) and the parallel C–C stretching mode ν(C–C) respectively. The weaker band at 1100 cm^{-1} is attributed to the C–N stretching mode ν(C–N). Our simulated Raman spectrum of Ag$_{13}$–PNTP is consistent with the observed spectrum of PNTP adsorbed on silver nanoparticles and bulk silver electrodes at relatively positive potentials.[50,54] These characteristic bands are observed at 1082, 1110, 1346 and 1573 cm^{-1}.

The simulated Raman spectrum of Ag$_{13}$–PATP is dominated by strong bands at 1074 and 1605 cm^{-1}. They are in a good

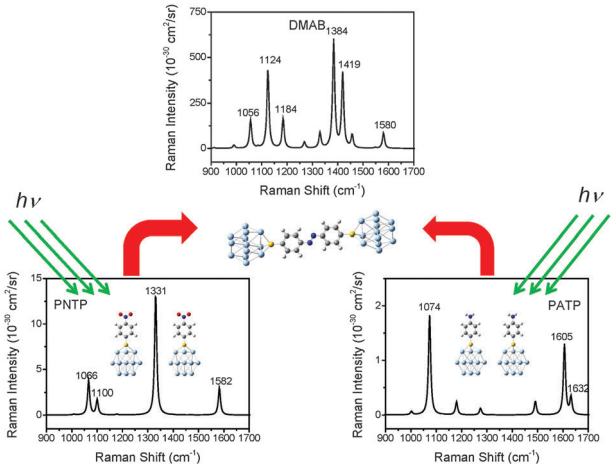

Fig. 1 Simulated Raman spectra of PNTP, PATP (B3LYP/6-311+G(d,p)/LANL2DZ) and DMAB (PW91PW91/6-311+G(d,p)/LANL2DZ) adsorbed on a silver surface.

agreement with those observed at 1078 and 1595 cm^{-1},[31] assigned to the C–S stretching mode ν(C–S) and the parallel C–C stretching mode, respectively. The weaker bands at 1275 and 1632 cm^{-1} are assigned to the C–N stretching mode ν(C–N) and the amine scissoring mode δ(NH$_2$), while the bands at 1180 and 1491 cm^{-1} can be attributed to C–H in-plane bending modes. Our calculated spectrum is in agreement with experimental results obtained under the conditions of acidic solution, low laser power density,[30,31] or near infrared excitation.[28,29]

As the nitro group is reduced to the amine group, the most significant changes reflected in the Raman spectra are the disappearance of the nitro symmetric stretching mode ν_s(NO$_2$) at 1331 cm^{-1} and the appearance of the amine scissoring mode δ(NH$_2$) at 1632 cm^{-1}. Meanwhile, the vibrational peaks relate to ν(C–N) and ν(C–C) blueshift from 1100 and 1582 cm^{-1} in PNTP to 1275 and 1605 cm^{-1} in PATP. The blue shift of ν(C–N) is consistent with a decrease in the C–N bond length from 1.471 Å in Ag$_{13}$–PNTP to 1.397 Å in Ag$_{13}$–PATP in the present calculation.

The simulated Raman spectrum of Ag$_{13}$–DMAB–Ag$_{13}$ in Fig. 1 agrees with experimental SERS spectra obtained from the PNTP on the silver system during electrochemical[53,55] and photochemical[20,23,56] reduction. We note that our simulations also reproduce the unusually intense peaks seen in SERS spectra of PATP on silver which, previously, were thought to result from CT enhancement.[24] This agrees with recent theoretical results with small silver and gold clusters though these peaks were interpreted due to the charge transfer enhancement from the Herzberg–Heller vibronic coupling effect.[32,57] Based on normal mode analysis, the peak at 1056 cm^{-1} is assigned to the C–S stretching mode. The peaks at 1124 and 1184 cm^{-1} are assigned to mixed vibrations from C–N stretching and C–H in-plane bending. The peaks at 1384 and 1419 cm^{-1} are assigned to mixed vibrations from N=N stretching, C–C stretching and C–H in-plane bending. Finally, the peak at 1580 cm^{-1} is assigned to the parallel C–C symmetric stretching mode. If we assume that DMAB remains in the C_{2h} symmetry point group, all of the most intense

Raman peaks (1124, 1384 and 1419 cm^{-1}) belong to the A_g irreducible representation.

Compared with silver, PNTP does not undergo such a photoreaction on a gold surface with visible light,[58] indicating that gold surfaces are of lower photochemical activity than silver surfaces. As shown in Fig. 1, for DMAB interacting with Ag_{13} clusters, the Raman intensities of the peaks predicted 1124, 1384, and 1419 cm^{-1} and observed at 1143, 1392 and 1436 cm^{-1} are significantly stronger than those calculated from PNTP and PATP. These can be further enhanced when one considers the resonance Raman enhancement effect. For the Ag_{13}–DMAB–Ag_{13} complex, we predicted that the low-lying charge transfer state was at 1.85 eV with oscillator strength about 0.1487 from the Ag_{13} clusters to DMAB molecules mixed with the excitation of DMAB itself. This is in agreement with the experimental observation that the charge transfer direction is from the metal to the molecule.[24] This interprets why the significant chemical enhancement was observed for PATP adsorbed on silver surfaces.

Surface Raman spectra of PNBA and PABA

In previous experimental studies, it was proposed that PNBA and PABA on rough silver surfaces convert to aromatic azo compounds and thus yield greatly intense Raman signals.[17,19,21,25] Fig. 2 shows the simulated Raman spectra of Ag_9–PNBA, Ag_9–PABA and Ag_9–ADBA–Ag_9. This is for the first time the DFT simulated Raman spectra of the studied system. Theoretical and experimental data for the normal Raman spectra and the SERS spectra of PNBA and PABA are compared in Tables S2 and S3 of the ESI.† Indeed, the match between our calculated and observed spectra provides strong evidence that PNBA and PABA can be transformed into the aromatic azo compound on silver surfaces.

The calculated Raman spectrum of Ag_9–PNBA in Fig. 2 has two strong bands at 1339 and 1604 cm^{-1}, medium intensity bands at 861, 1094 and 1370 cm^{-1}, and weak bands at 820, 1130 and 1525 cm^{-1}. The peaks predicted at 1339 and 1370 cm^{-1} are assigned to the symmetric stretches of the nitro and carboxylate groups respectively. These calculated frequencies

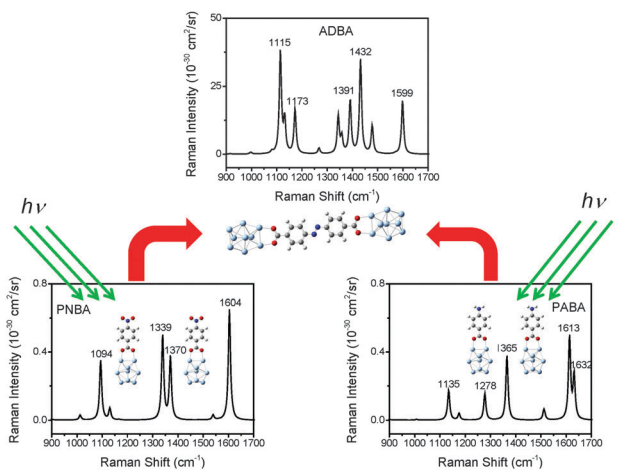

Fig. 2 Simulated Raman spectra of PNBA, PABA (B3LYP/6-311+G(d,p)/LANL2DZ) and ADBA (PW91PW91/6-311+G(d, p)/LANL2DZ) adsorbed on a silver surface.

are slightly lower than the experimentally obtained values of 1355 and 1395 cm^{-1}.[17] The medium intensity peak at 1094 cm^{-1} and the weak band at 1130 cm^{-1} are assigned to C–NO_2 and C–CO_2 stretches coupled with C–H in-plane bending. The strong peak at 1604 cm^{-1} is assigned to the ring C–C stretching vibration. The weak bands at 1525 and 1617 cm^{-1} are assigned to the asymmetric stretching vibrations of the nitro and carboxylate groups, respectively (the band at 1617 cm^{-1} is so weak that it is completely hidden by the strong band at 1604 cm^{-1}). The medium intensity peak at 861 cm^{-1} and the weak band at 820 cm^{-1} are assigned to the bending modes of nitro and carboxylate groups, respectively.

The calculated Raman spectrum of Ag_9–PABA is characterized by strong bands at 1365 and 1613 cm^{-1}, medium intensity bands at 1135, 1278 and 1632 cm^{-1}, and weak bands at 1176 and 1512 cm^{-1}. The peaks which are due to C–CO_2 stretching (1135 cm^{-1}), C–O symmetric stretching (1365 cm^{-1}) and C–C stretching (1613 cm^{-1}) all occur at roughly the same positions for PABA as that for PNBA. However, the C–NH_2 stretching frequency shows a blueshift from 1130 cm^{-1} to 1278 cm^{-1} and this is in agreement with a decrease in C–N bond length. The experimentally obtained C–N stretching peak occurs at 1253 cm^{-1}, 25 cm^{-1} lower than our calculated value. This redshift is due to an interaction between the amine group and silver.[59] The medium intensity peak at 1632 cm^{-1} is assigned to NH_2 scissoring vibration. Venkatachalam *et al.* observed NH_2 scissoring at 1630 cm^{-1} in IR spectra of PABA.[25] They found that this band disappears after PABA is exposed to air for 1 hour, and suggested that PABA is transformed to ADBA.

Two very different SERS spectra may be obtained for PNBA and PABA on silver. One is similar to the normal Raman spectrum of each molecule. The other spectrum is the same for both these molecules, and it has strong bands at 1142, 1390 and 1437 cm^{-1}. Roth *et al.* considered these unusual SERS peaks to be the result of photochemical reactions of PNBA and PABA on silver.[17,25] They attributed the band near 1460 cm^{-1} and the doublet bands near 1150 cm^{-1} to ADBA formed by the reductive dimerization of PNBA and oxidative dimerization of PABA under laser irradiation. The simulated Raman spectrum of Ag_9–ADBA–Ag_9 which we present in Fig. 2 strongly resembles the unusual SERS spectra obtained from PNBA and PABA on silver, and reproduces well the SERS spectrum obtained from synthesized sodium ADBA on silver.[25] The peaks at 1391 and 1432 cm^{-1} are assigned to N=N stretching coupled with C–C stretching. The peaks at 1115 and 1173 cm^{-1} are assigned to C–N stretching coupled with C–H in-plane bending. They are closely associated with the azo group, >C–N=N–C<. The peak at 1599 cm^{-1} is assigned to C–C symmetric stretching in two benzene rings. The symmetric stretching mode of the carboxylate groups shifts to 1344 cm^{-1}.

Photo-induced surface catalytic coupling reactions

By inspecting our simulated spectra with experimentally obtained spectra in the literature, we contend that PNTP, PATP, PNBA and PABA on silver undergo photoinduced surface catalytic coupling reactions and conversion to azobenzene derivatives.

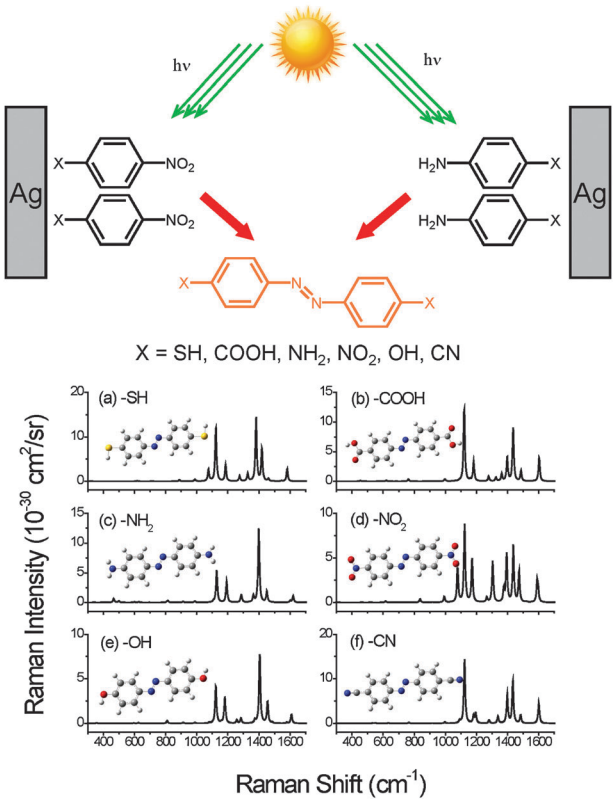

Fig. 3 Raman spectra of azobenzene derivatives with various *para* functional groups simulated by PW91PW91/6-311+G(d, p): (a) –SH, (b) –COOH, (c) $–NH_2$, (d) $–NO_2$, (e) –OH and (f) –CN.

These latter surface species give characteristic SERS signals of interest. We have noted that the dimerization processes occurred while SERS measurements were made on a number of nitrobenzene and aniline derivatives, including 1,4-dinitrobenzene,[60] *p*-nitro(pyridine *N*-oxide),[61] *p*-nitrobenzonitrile,[62,63] *p*-nitroaniline,[64–67] *p*-nitrophenol,[68] *o*-aminothiophenol,[69] *o*-aminophenol,[70,71] *o*-phenylenediamine[72] and *p*-phenylenediamine.[66] Here, SERS bands were often assigned to vibrations of the initially present probe molecules. Fig. 3 shows the simulated Raman spectra of different azobenzene derivatives with various *para* functional groups. All of these compounds exhibit strong Raman signals at around 1130, 1190, 1390 and 1430 cm^{-1}. Our calculated results explain well the SERS signals observed in many systems comprising a nitrobenzene or aniline derivative adsorbed on a silver surface. On the basis of normal mode analysis, band assignments for these peaks are listed according to the potential energy distributions in Table S4 of the ESI.† The peaks at about 1130 and 1190 cm^{-1} are assigned to C–N stretching coupled with C–H in-plane bending, while the peaks at about 1390 and 1430 cm^{-1} are attributed to N=N stretching and C–C stretching coupled with C–H in-plane bending.

For Fig. 3, we note that these vibrational frequencies are not very sensitive to the nature of the *para* functional groups. However, the N=N stretching frequency in *para*-substituted azobenzene is lower than that in azobenzene.[73] We also note that the relative intensities of the peaks at about 1390 and 1430 cm^{-1} depend on the electronic properties of the *para* functional groups. For electron-donating groups such as (a) thiol, (c) amine and (e) hydroxyl, the peak at about 1390 cm^{-1} is stronger than the peak at about 1430 cm^{-1}. For electron-withdrawing groups such as (b) carboxylic acid, (d) nitro and (f) nitrile, the peak at around 1430 cm^{-1} is stronger than the peak at around 1390 cm^{-1}. This is in agreement with our theoretical analysis, showing that the N=N stretching is dominant in the 1390 cm^{-1} vibration of (a), (c) and (e), and in the 1430 cm^{-1} vibration of (b), (d) and (f). Since the Raman signals at around 1130, 1190, 1390 and 1430 cm^{-1} are so intense, we suggest that they can be used to identify reaction products and investigate reaction mechanisms.

Discussion

Electronic structures of $ArNO_2$ and $ArNH_2$

As we have already indicated, nitrobenzene and aniline derivatives can be converted into azobenzene derivatives and display very intense SERS signals. The transformation of nitrobenzene and aniline derivatives into azo compounds should occur by a photo-induced surface catalytic coupling reaction.[31,35] To investigate the reaction mechanism, we first study the difference in electronic structures of nitrobenzene and aniline.

Fig. 4 presents the frontier molecular orbitals of nitrobenzene and aniline formed from a linear combination of benzene ring orbitals with the nitro group π* antibonding orbital and the amine group lone pair (LP) orbital. The HOMO and LUMO of benzene are each two degenerate orbitals with energies of −7.07 and −0.46 eV, relative to the vacuum energy level, respectively. According to molecular orbital theory, the energy level of a nitro group π* orbital is close to the benzene LUMO and the nitrobenzene LUMO drops down to −2.91 eV because of orbital interaction. For aniline, the HOMO rises to −5.77 eV as a result of the interaction between benzene's HOMO and the amine group's LP orbital.

Table 1 shows that the *para* functional group will further influence the HOMO and LUMO energy levels in nitrobenzene and aniline derivatives. Electron-withdrawing groups lead to a decrease in the energy levels of the frontier orbitals while electron-donating groups have the opposite effect. The energy levels increase in order from the most strongly electron-withdrawing

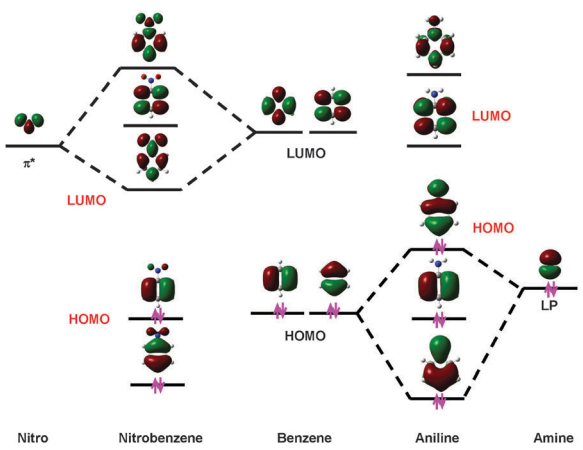

Fig. 4 Frontier molecular orbitals of nitrobenzene and aniline formed by interaction of the benzene ring with the nitro and amine groups.

Table 1 Calculated HOMO and LUMO energy levels (eV) for nitrobenzene, aniline and their *para*-substituted derivatives obtained with B3LYP/6-311+G(d,p)

	$ArNO_2$		$ArNH_2$	
Substituted group	HOMO	LUMO	HOMO	LUMO
$-NO_2$	−8.71	−3.92	−6.64	−2.48
–CN	−8.46	−3.59	−6.37	−1.28
–COOH	−8.25	−3.37	−6.20	−1.31
–Cl	−7.87	−3.11	−5.90	−0.73
–Br	−7.71	−3.12	−5.90	−0.76
–H	−7.95	−2.91	−5.77	−0.46
$-CH_3$	−7.70	−2.79	−5.58	−0.33
–OH	−7.34	−2.72	−5.42	−0.49
–SH	−6.99	−2.88	−5.99	−0.60
$-NH_2$	−6.64	−2.44	−5.04	−0.34

group ($-NO_2$) to the most strongly electron-donating group ($-NH_2$). The electrochemical reduction process is closely associated with the LUMO of the electro-active centre. The LUMO of PNTP (−2.88 eV) is higher than that of PNBA (−3.37 eV). This is in agreement with the cyclic voltammograms of PNTP and PNBA on silver electrodes, where the initial reduction potential of PNTP is around −0.9 V (*vs.* SCE in 0.1 M $NaClO_4$)[53] and the initial reduction potential of PNBA is around −0.55 V (*vs.* SCE in 0.1 M Na_2SO_4).[18] Thus, the lower the electron affinity level, the easier the reduction during cathode polarization. The HOMO of PABA (−6.20 eV) is lower than that of PATP (−5.99 eV), which means PATP is easier to be oxidized than PABA.

Photon-driven CT excited states

The unique electronic structure of $ArNO_2$ and $ArNH_2$ derivatives results in different photoinduced CT directions when these molecules adsorb on silver surfaces. Fig. 5 presents the molecular orbitals involved in photon-driven CT processes for PNTP, PATP, PNBA, and PABA adsorbed on silver. The orbital IDs and details of TD-DFT results are listed in Tables S5 to S8 of the ESI.† Here we consider only the low-lying CT states having excitation energy less than the interband transition energy of silver. The LUMO energy levels of adsorbed PNTP and PNBA are −2.67 and −2.69 eV, and the HOMO energy levels of adsorbed PATP and PABA are

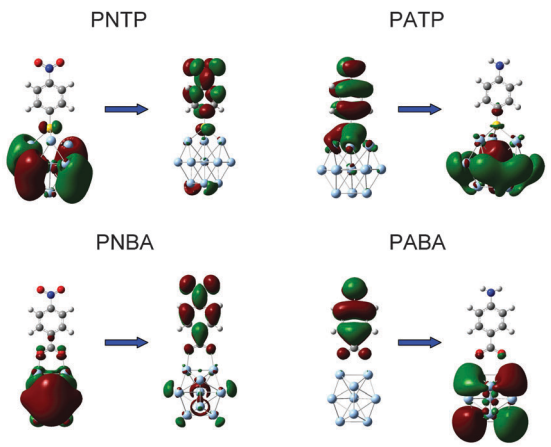

Fig. 5 Molecular orbitals of PNTP, PATP, PNBA and PABA interacting with silver clusters during photon-driven CT.

Table 2 Vertical transition energies (ΔE in eV) and oscillator strengths (f) for the first and second charge transfer states of PNTP, PATP, PNBA and PABA on silver calculated with TD-B3LYP/6-311+G(d,p)

Molecule	$\Delta E(CT_1)$	$f(CT_1)$	$\Delta E(CT_2)$	$f(CT_2)$	Assignment[a]
Ag_{13}–PNTP	1.74	0.0001	1.76	0.0508	M → m
Ag_{13}–PATP	2.28	0.0006	2.39	0.0034	m → M
Ag_9–PNBA	2.00	0.0031	2.29	0.0072	M → m
Ag_9–PABA	2.21	0.0001	2.64	0.0274	m → M

[a] M, metal; m, molecule.

−5.52 and −5.63 eV. They are close to the Fermi level of silver, which is −4.3 eV. It is shown in Fig. 5 that photon-driven CT occurs from the occupied silver 5s orbital to the LUMO of adsorbed PNTP or PNBA. For PATP or PABA on silver, the CT occurs from the adsorbate HOMO to the unoccupied orbital of the silver cluster. Thus, CT transitions for nitrobenzene derivatives are from the metal to the molecule, while for aniline derivatives they are from the molecule to the metal.

Table 2 summarizes the calculated vertical transition energies and oscillator strengths of the first and second CT states. The vertical transition energies of the first CT state for these surface complexes range from 1.74 to 2.28 eV, and these values are close to the excitation energy range generally used when SERS measurements are made on nanostructured silver. The CT transition energies of PNTP and PNBA are lower than those of PATP and PABA. The second CT state has the same transition assignments, but its oscillator strengths are larger than those of the first CT state. For adsorbed PNTP and PNBA, the low-lying CT transitions occur from different occupied orbitals of the silver cluster to the LUMO of the molecule. For adsorbed PATP and PABA, the low-lying CT transitions occur from the molecular HOMO to an unoccupied silver cluster orbital. Although the CT transition oscillator strengths are quite small, the existence of CT transition states will directly influence SERS relative intensity. It is worth noting that the predicted CT direction is opposite to the experimental observation for PATP adsorbed on a silver electrode. Even though the CT direction is reasonable, it is also impossible to yield abnormal SERS peaks observed in SERS measurements due to the lack of corresponding fundamental bands. Our previous study shown that there are no vibrational fundamentals in adsorbed PATP corresponding well to the peaks at 1142, 1391, or 1440 cm^{-1}, as observed in many SERS spectra.[35] Within the range of 1325–1495 cm^{-1} there is only one fundamental (ν_{19b}) predicted at 1423 cm^{-1}.

Mechanisms of photoinduced surface catalytic coupling reactions

Light incident on molecules adsorbed on a roughened Ag surface or on colloidal Ag involves both surface plasmon and CT processes. The directly photoinduced CT and the subsequent photochemical reaction channel are schematically depicted in Fig. 6. The metal electrode can be considered a source of electrons for reduction reactions or an electron sink for oxidation reactions. The Fermi level of the silver is located between the HOMO and LUMO of the adsorbate, and it can be tuned by applying a potential. A negatively applied

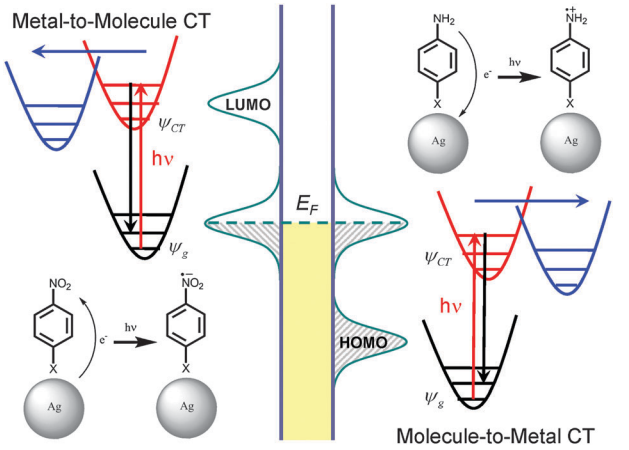

Fig. 6 Schematic diagram of the photoinduced electron transfer and subsequent photochemical reaction for aromatic nitro and amine compounds adsorbed on silver surfaces. Left: an electron is excited from the Fermi level of the metal to the LUMO of the molecule, which leads to a photochemical reduction of aromatic nitro compounds on silver. Right: an electron is excited from the HOMO of the molecule to the Fermi level of the metal, which leads to a photochemical oxidation of aromatic amine compounds on silver.

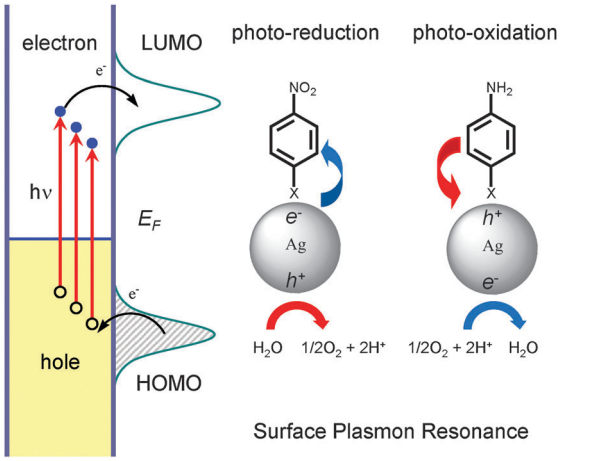

Fig. 7 Schematic diagram of electron–hole separation by excitation of surface plasmon on silver nanostructures and subsequent photochemical reaction at metal–molecule interfaces. Left: electron–hole pairs are created by surface plasmon resonance. A hot electron is transferred to the molecular LUMO and a hot hole captures an electron from the molecular HOMO. Right: hot-electron induced photo-reduction of $ArNO_2$ and hot-hole induced photo-oxidation of $ArNH_2$.

potential will raise the Fermi level and a positive one will lower it. When the energy difference between the ground state ψ_g and the photon-driven CT excited state ψ_{CT} matches the energy of the exciting radiation, a resonant CT will take place. As we have already explained above, electron transfer occurs from silver to the molecule for X–$ArNO_2$ and from the molecule to silver for X–$ArNH_2$ (here X denotes the *para* functional group). The excited surface complex may then undergo one of the two different types of deexcitation. One involves a reverse CT back to the ground state, followed by a radiative process. Raman scattering or fluorescence emission may be involved in this purely physical deexcitation. The other possibility is a photochemical reaction. The excited nitro radical anion may pick up a proton from the proton donor in solution to form a neutral $ArNO_2H$ radical which then undergoes further reaction. The excited amine radical cation may lose a proton to form a neutral ArNH radical which can dimerize through a nitrogen–nitrogen coupling reaction.

Fig. 7 illustrates another CT mechanism. Here the electron transfer process is divided into two steps. In the first step, absorption of light by the metal creates an electron–hole pair through surface plasmon activity. The hot electron then tunnels out of the surface and is injected into the LUMO of the adsorbed molecule, and the holes will be quenched by water as a sacrificial electron donor. Similarly, a hot hole in the metal can capture an electron from the adsorbate HOMO, the hot electrons will be quenched by oxygen or other oxidant. Here plasmonic silver nanostructures act as catalysts to transform light energy to chemical energy. The larger Ag nanoparticles have close to a continuum of filled metal states and excitations which support both surface plasmon and CT processes simultaneously will give the highest photochemical cross-section.

The excitation of surface plasmons in noble metal nanostructures by visible light is a very efficient process, and there are indeed other examples of surface plasmon induced chemical reactions in the literature. The rates of catalytic oxidation reactions on silver nanostructures were found to be strongly dependent on the wavelength of incident light, peaking at the surface plasmon resonance wavelength.[5] Noble metal nanoparticles (mainly silver and gold) show excellent catalytic activity in visible light for water splitting[6,7] and Fenton's reaction.[9]

Selectivity of photoinduced coupling reactions

The proposed photochemical reactions of X–$ArNO_2$ and X–$ArNH_2$ under visible light are shown in Fig. 8. Formation of reaction intermediates ArNO, ArNHOH, ArN(O)–NAr and ArNH–NHAr during reduction of $ArNO_2$ and oxidation of $ArNH_2$ are shown in Fig. 9. Vertical transition energies, excitation wavelengths and oscillator strengths are presented for the CT excited states in Table 3.

During the photochemical reduction of X–$ArNO_2$, an electron is excited from silver to the π^* orbital of the adsorbate and X–$ArNO_2$ is reduced to X–ArNHOH through X–ArNO in a series of electron and proton transfer steps. The direction of CT is silver-to-molecule for X–ArNO and molecule-to-silver for X–ArNHOH as shown in Fig. 9. Thus, reduction of ArNO and oxidation of ArNHOH are reversible processes during the photoreduction of $ArNO_2$. This is in agreement with what is observed for the reversible redox couple ArNO/ArNHOH in electrochemistry.[18,74–76] At more negative applied potentials, ArNHOH can be reduced to $ArNH_2$. Under photochemical conditions, however, the ArNHOH LUMO is higher than the $ArNO_2$ and ArNO LUMOs and CT from silver to ArNHOH is difficult to achieve with visible light. The excitation energies required for metal-to-molecule CT in PHATP and PHABA are 3.32 and 3.97 eV, respectively, so ArNHOH will not be further reduced to $ArNH_2$ during a typical SERS measurement. In neutral and alkaline solutions, ArNO and ArNHOH can undergo a condensation reaction on the silver surface to form an azoxy compound. Fig. 8 shows that azoxybenzene can be

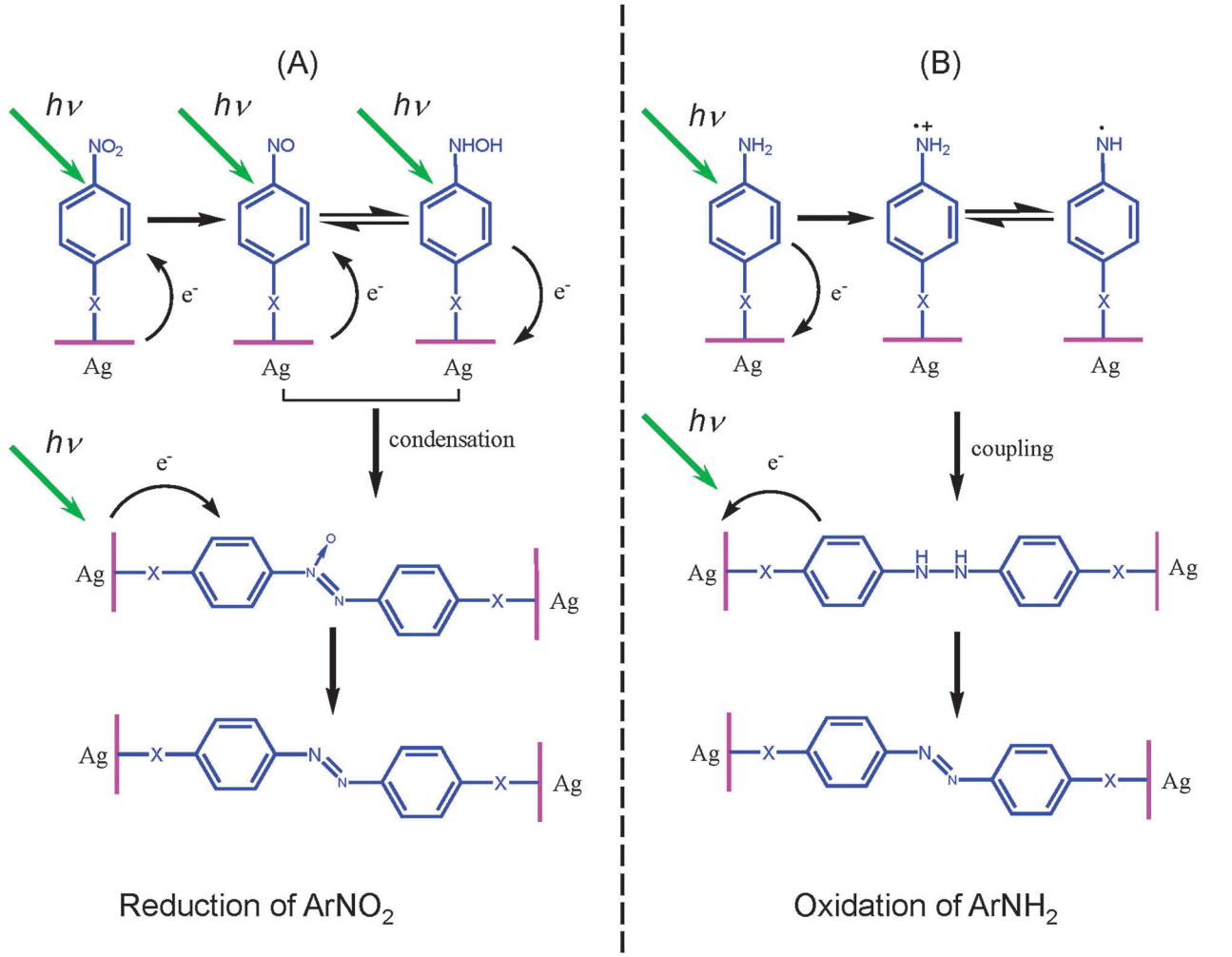

Fig. 8 Reaction mechanisms for the photochemical reduction of $ArNO_2$ (A) and photochemical oxidation of $ArNH_2$ (B) on silver. In both cases, azobenzene derivatives are produced by surface catalytic coupling reactions.

further reduced to azobenzene under visible light irradiation as the electron transfer occurs from the metal to the adsorbate.

The reaction route for photoreduction of $ArNO_2$ under visible light is quite different from its electrochemical reduction in which two different routes are involved. In one route, the aromatic nitro compound can be directly reduced to amine compound through nitroso and hydroxylamine compounds. The second route involves condensation of the nitroso compound with a nucleophilic hydroxylamine to give an azoxy compound, which is reduced in a series of consecutive reactions to azo, hydrazo and amine compounds.[18,74,75] However, in photoreduction of $ArNO_2$ the Raman excitation light energy is insufficient to drive the reduction from hydroxylamine to aniline. The direct reduction from $ArNO_2$ to $ArNH_2$ does not happen within visible light irradiation. Only azobenzene derivatives can be formed through the condensation pathway, as mentioned above. Therefore, the photochemical reductions of aromatic nitrobenzenes on silver under visible light are of unique selectivity in chemical reactions.

For photochemical oxidation of $ArNH_2$, an electron is excited from the adsorbate HOMO to the silver Fermi level. $ArNH_2$ is oxidized to a radical cation, but an equilibrium exists between the radical cation form and the neutral radical one dependent on the pH in aqueous solution. In basic medium the $ArNH_2^{+\bullet}$ radical cation can be deprotonated to produce an $ArNH^{\bullet}$ neutral radical. In acidic medium the radical cation reacts with its resonance structure in tail-to-tail and head-to-tail coupling to form benzidine and *N*-phenyl-1,4-phenylenediamine.[77,78] The head-to-head coupling does not occur to any great extent because a strong electrostatic repulsion exists between radical cations. The electrochemistry of PATP in acidic solution has also been studied.[79–81] Cyclic voltammetry, XPS and FTIR spectroscopy show that PATP molecules adsorbed on electrode surfaces undergo electrochemical oxidation to produce radical cations, which then couple to form the head-to-tail product.[80,81] In basic solution, the main single electron oxidation product of $ArNH_2$ should be the $ArNH^{\bullet}$ neutral radical. The $ArNH^{\bullet}$ radical then undergoes head-to-head coupling to form hydrazobenzene, which can be further oxidized by exciting an electron in the HOMO of the molecule to the metal electrode to produce azobenzene species as shown in Fig. 8 and 9.

Table 4 presents the calculated Gibbs free energies of formation of DMAB (ADBA) from PNTP (PNBA) and

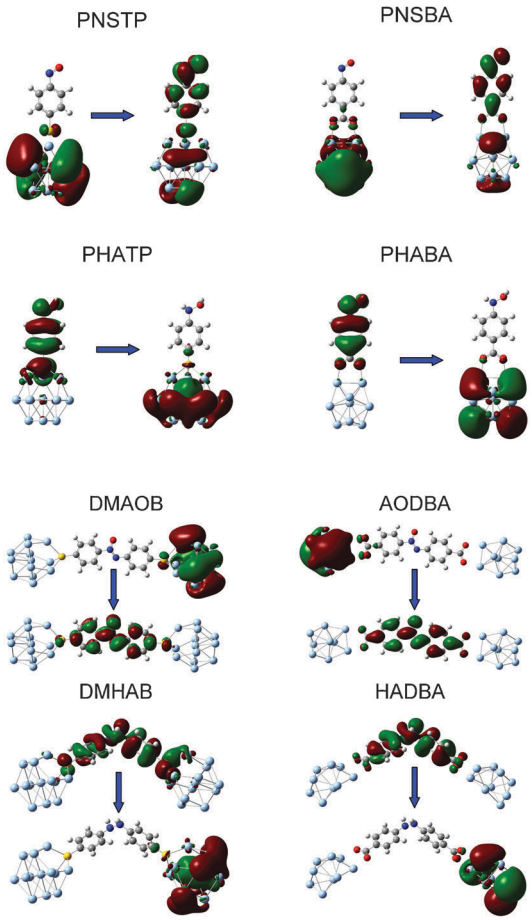

Fig. 9 Molecular orbitals involved in photon-driven CT for *p*-nitrosothiophenol (PNSTP), *p*-nitrosobenzoic acid (PNSBA), *p*-hydroxylaminethiophenol (PHATP), *p*-hydroxylaminebenzoic acid (PHABA), *p*,*p*′-dimercaptoazoxybenzene (DMAOB), *p*,*p*′-azoxydibenzoic acid (AODBA), *p*,*p*′-dimercaptohydrazobenzene (DMHAB), and *p*,*p*′-hydrazodibenzoic acid (HADBA) interacting with silver clusters.

Table 3 Vertical transition energies (ΔE in eV), excitation wavelengths (λ in nm) and oscillator strengths (f) of the first charge transfer states of PNSTP, PHATP, PNSBA, PHABA, DMAOB, DMHAB, AODBA and HADBA on silver calculated with TD-B3LYP/6-311+G(d,p)

Molecule	ΔE(CT)	λ(CT)	f(CT)	Assignment[a]
Ag_{13}–PNSTP	1.581	784	0.0004	M → m
Ag_{13}–PHATP	2.403	516	0.0013	m → M
Ag_9–PNSBA	2.077	597	0.0034	M → m
Ag_9–PHABA	2.418	513	0.0000	m → M
Ag_{13}–DMAOB–Ag_{13}	1.853	669	0.1050	M → m
Ag_{13}–DMHAB–Ag_{13}	2.329	532	0.0002	m → M
Ag_9–AODBA–Ag_9	2.457	505	0.0155	M → m
Ag_9–HADBA–Ag_9	2.196	565	0.0001	m → M

[a] M, metal; m, molecule.

PATP (PABA). Here hydrogen is the reductant of $ArNO_2$ reduction while oxygen is the oxidant of $ArNH_2$ oxidation. It is found that the transformations from $ArNO_2$ and $ArNH_2$ to azobenzene species are spontaneous process since the Gibbs free energies are negative.

When X–$ArNO_2$ and X–$ArNH_2$ are converted to azobenzene derivatives on silver, characteristic Raman bands should be seen at around 1130, 1390, and 1430 cm^{-1}. The transformation depends on laser wavelength,[28,29] irradiation power,[17,25,30,31] and pH of the solution.[26,32–34]

Table 4 Calculated Gibbs free energies of formation of azobenzene derivatives from $ArNO_2$ and $ArNH_2$ on silver at the B3LYP/6-311+G(d,p) level

Reaction	ΔG (kcal mol^{-1})
$2Ag_{13}$–PNTP + $4H_2$ → Ag_{13}–DMAB–Ag_{13} + $4H_2O$	−151.87
$2Ag_{13}$–PATP + O_2 → Ag_{13}–DMAB–Ag_{13} + $2H_2O$	−51.56
$2Ag_9$–PNBA + $4H_2$ → Ag_9–ADBA–Ag_9 + $4H_2O$	−151.41
$2Ag_9$–PABA + O_2 → Ag_9–ADBA–Ag_9 + $2H_2O$	−48.48

The thermodynamics of the photochemical reaction are determined by the excitation energy. If the excitation energy matches the gap between the ground state and the CT excited state, a photon-driven electron transfer will take place from the molecule to the metal or from the metal to the molecule dependent on the relative position of the HOMO and LUMO of adsorbed molecules. This will induce the photo-oxidation or reduction reaction. Wang *et al.*[28] and Richter *et al.*[29] studied the wavelength-dependent SERS of PATP on silver. They found that with an excitation wavelength of 1064 nm, the SERS spectrum of PATP was comparable to its normal Raman spectrum. On the other hand, intense Raman bands from the photochemical reaction product DMAB appeared with an excitation wavelength of 514.5 nm.

The kinetics of the photochemical reaction is determined by the irradiation power. The number of molecules undergoing CT, and therefore the rate of dimerization, will increase with laser power.[18] Furthermore, photochemical reactions often require a finite accumulation of energy in the molecule before the desired process can take place.[11] Increasing the power of irradiation can lead to localized heating of the substrate and induce thermal reactions. Roth *et al.*[17] and Venkatachalam *et al.*[25] found that PNBA and PABA adsorbed on silver islands transform into ADBA during laser irradiation at high power. They found heating PNBA up to 160 °C did not produce azobibenzoate although they eventually invoke a laser induced thermal mechanism. Sun *et al.* found that the photoreaction rate of PNBA is proportional to excitation power, indicating that laser heating is not the source of the photochemical reaction.[18] Huang *et al.* demonstrated that the transformation of PATP to DMAB can be efficiently suppressed by using a laser with an ultra low power density.[31]

Solution pH influences the $ArNO_2$ reduction and $ArNH_2$ oxidation pathways. The formation of azobenzene species is favored in alkaline medium (*e.g.*, characteristic Raman signals from DMAB were recorded after PATP was added to silver in basic solution,[26,32–34] and Holze observed similar pH-dependent SERS phenomena for *p*-nitroaniline adsorbed on silver and gold electrodes[64]). In acidic medium, $ArNO_2$ is electrochemically reduced to $ArNH_2$ through ArNO and ArNHOH, while $ArNH_2$ is oxidized tail-to-tail or head-to-tail to produce benzidine or *N*-phenyl-1,4-phenylenediamine.

Conclusions

We have shown that azobenzene derivatives can be produced from aromatic nitro and amine compounds on nanostructured

silver through photoinduced surface catalytic coupling reactions. Simulated Raman spectra indicate PNTP and PNBA undergo reductive coupling reactions while PATP and PABA undergo oxidative coupling reactions to produce DMAB and ADBA. The transformation also occurs for other aromatic nitro and amine compounds on nanostructured silver surfaces. The resulting azobenzenes exhibit characteristic Raman signals which are quite different from those of the *para*-substituted $ArNO_2$ and $ArNH_2$ reactants.

A photoinduced charge transfer model is presented to explain the transformations observed in $ArNO_2$ and $ArNH_2$ on nanostructured silver. TD-DFT calculations show that electron excitation occurs from silver to the LUMO of the adsorbed $ArNO_2$ molecule, and from the HOMO of the adsorbed $ArNH_2$ molecule to silver. $ArNO_2$ and $ArNH_2$ can subsequently react from the charge transfer excited state to produce azobenzene derivatives. The reaction pathways strongly depend on the excitation energy, irradiation power, and solution pH. The reduction of $ArNO_2$ and oxidation of $ArNH_2$ are complex reactions which involve multistep electron transfer and proton transfer processes. Systematic studies of the thermodynamics and kinetics are now underway in our group. Finally, we believe that the present results may provide a new strategy for the syntheses of aromatic azo dyes from aromatic nitro and amine compounds on nanostructured silver, where surface plasmon resonance is quite efficient and enhances photoinduced charge transfer processes.

Acknowledgements

We are grateful for the financial support of this work by the Ministry of Science and Technology of China (973 Program No. 2009CB930703), and by the NSF of China (Nos. 91027009, 21021002 and 20973143). DYW also thanks the HPC of Xiamen University for support (2010121020).

Notes and references

1 P. V. Kamat, *J. Phys. Chem. C*, 2007, **111**, 2834–2860.
2 M. Moskovits, *Rev. Mod. Phys.*, 1985, **57**, 783.
3 L. Brus, *Acc. Chem. Res.*, 2008, **41**, 1742–1749.
4 W. L. Barnes, A. Dereux and T. W. Ebbesen, *Nature*, 2003, **424**, 824–830.
5 P. Christopher, H. Xin and S. Linic, *Nat. Chem.*, 2011, **3**, 467–472.
6 D. B. Ingram and S. Linic, *J. Am. Chem. Soc.*, 2011, **133**, 5202–5205.
7 C. Gomes Silva, R. Juárez, T. Marino, R. Molinari and H. García, *J. Am. Chem. Soc.*, 2011, **133**, 595–602.
8 H. Zhu, X. Ke, X. Yang, S. Sarina and H. Liu, *Angew. Chem., Int. Ed.*, 2010, **49**, 9657–9661.
9 S. Navalon, M. de Miguel, R. Martin, M. Alvaro and H. Garcia, *J. Am. Chem. Soc.*, 2011, **133**, 2218–2226.
10 A. Nitzan and L. E. Brus, *J. Chem. Phys.*, 1981, **74**, 5321–5322.
11 A. Nitzan and L. E. Brus, *J. Chem. Phys.*, 1981, **75**, 2205–2214.
12 C. J. Chen and R. M. Osgood, *Phys. Rev. Lett.*, 1983, **50**, 1705–1708.
13 G. M. Goncher, C. A. Parsons and C. B. Harris, *J. Phys. Chem.*, 1984, **88**, 4200–4209.
14 R. A. Wolkow and M. Moskovits, *J. Chem. Phys.*, 1987, **87**, 5858–5869.
15 R. T. Kidd, D. Lennon and S. R. Meech, *J. Chem. Phys.*, 2000, **113**, 8276–8282.
16 A. O. Govorov and H. H. Richardson, *Nano Today*, 2007, **2**, 30–38.
17 P. G. Roth, R. S. Venkatachalam and F. J. Boerio, *J. Chem. Phys.*, 1986, **85**, 1150–1155.
18 S. Sun, R. L. Birke, J. R. Lombardi, K. P. Leung and A. Z. Genack, *J. Phys. Chem.*, 1988, **92**, 5965–5972.
19 X. M. Yang, D. A. Tryk, K. Hashimoto and A. Fujishima, *J. Phys. Chem. B*, 1998, **102**, 4933–4943.
20 N. Matsuda, T. Sawaguchi, M. Osawa and I. Uchida, *Chem. Lett.*, 1995, **24**, 145–146.
21 X. M. Yang, D. A. Tryk, K. Ajito, K. Hashimoto and A. Fujishima, *Langmuir*, 1996, **12**, 5525–5527.
22 K. Kim, S. J. Lee and K. L. Kim, *J. Phys. Chem. B*, 2004, **108**, 16208–16212.
23 B. Dong, Y. Fang, L. Xia, H. Xu and M. Sun, *J. Raman Spectrosc.*, 2011, **42**, 1205–1206.
24 M. Osawa, N. Matsuda, K. Yoshii and I. Uchida, *J. Phys. Chem.*, 1994, **98**, 12702.
25 R. S. Venkatachalam, F. J. Boerio and P. G. Roth, *J. Raman Spectrosc.*, 1988, **19**, 281–287.
26 W. Hill and B. Wehling, *J. Phys. Chem.*, 1993, **97**, 9451–9455.
27 X. M. Yang, D. A. Tryk, K. Hashimoto and A. Fujishima, *J. Raman Spectrosc.*, 1998, **29**, 725–732.
28 Y. Wang, X. Zou, W. Ren, W. Wang and E. Wang, *J. Phys. Chem. C*, 2007, **111**, 3259–3265.
29 A. P. Richter, J. R. Lombardi and B. Zhao, *J. Phys. Chem. C*, 2010, **114**, 1610–1614.
30 G. K. Liu, J. Hu, P. C. Zheng, G. L. Shen, J. H. Jiang, R. Q. Yu, Y. Cui and B. Ren, *J. Phys. Chem. C*, 2008, **112**, 6499–6508.
31 Y. F. Huang, H. P. Zhu, G. K. Liu, D. Y. Wu, B. Ren and Z. Q. Tian, *J. Am. Chem. Soc.*, 2010, **132**, 9244–9246.
32 M. Sun, Y. Huang, L. Xia, X. Chen and H. Xu, *J. Phys. Chem. C*, 2011, **115**, 9629–9636.
33 A. M. Gabudean, D. Biro and S. Astilean, *J. Mol. Struct.*, 2011, **993**, 420–424.
34 S. Zong, Z. Wang, J. Yang and Y. Cui, *Anal. Chem.*, 2011, **83**, 4178–4183.
35 D. Y. Wu, X. M. Liu, Y. F. Huang, B. Ren, X. Xu and Z. Q. Tian, *J. Phys. Chem. C*, 2009, **113**, 18212–18222.
36 D. Y. Wu, L. B. Zhao, X. M. Liu, R. Huang, Y. F. Huang, B. Ren and Z. Q. Tian, *Chem. Commun.*, 2011, **47**, 2520–2522.
37 K. Uetsuki, P. Verma, T. Yano, Y. Saito, T. Ichimura and S. Kawata, *J. Phys. Chem. C*, 2010, **114**, 7515–7520.
38 K. Kim, D. Shin, H. B. Lee and K. S. Shin, *Chem. Commun.*, 2011, **47**, 2020–2022.
39 L. B. Zhao, R. Huang, Y. F. Huang, D. Y. Wu, B. Ren and Z. Q. Tian, *J. Chem. Phys.*, 2011, **135**, 134707.
40 J. P. Perdew, K. Burke and Y. Wang, *Phys. Rev. B: Condens. Matter Mater. Phys.*, 1996, **54**, 16533.
41 J. P. Perdew, *Phys. Rev. B: Condens. Matter Mater. Phys.*, 1986, **33**, 8822.
42 A. D. Becke, *Phys. Rev. A: At., Mol., Opt. Phys.*, 1988, **38**, 3098.
43 C. Lee, W. Yang and R. G. Parr, *Phys. Rev. B: Condens. Matter Mater. Phys.*, 1988, **37**, 785–789.
44 A. D. Becke, *J. Chem. Phys.*, 1993, **98**, 5648–5652.
45 R. Krishnan, J. S. Binkley, R. Seeger and J. A. Pople, *J. Chem. Phys.*, 1980, **72**, 650–654.
46 A. D. McLean and G. S. Chandler, *J. Chem. Phys.*, 1980, **72**, 5639–5648.
47 P. J. Hay and W. R. Wadt, *J. Chem. Phys.*, 1985, **82**, 270–283.
48 W. R. Wadt and P. J. Hay, *J. Chem. Phys.*, 1985, **82**, 284–298.
49 M. J. Frisch, G. W. Trucks, H. B. Schlegel, G. E. Scuseria, M. A. Robb, J. A. Cheeseman, G. Scalmani, V. Barone, B. Mennucci, G. A. Petersson, H. Nakatsuji, M. Caricato, X. Li, H. P. Hratchian, A. F. Izmaylov, J. Bloino, G. Zheng, J. L. Sonnenberg, M. Hada, M. Ehara, K. Toyota, R. Fukuda, J. Hasegawa, M. Ishida, A. Nakajima, Y. Honda, O. Kitao, H. Nakai, T. Vreven, J. A. Montgomery, Jr., J. E. Peralta, F. Ogliaro, M. Bearpark, J. J. Heyd, E. Brothers, K. N. Kudin, V. N. Staroverov, R. Kobayashi, J. Normand, K. Raghavachari, A. Rendell, J. C. Burant, S. S. Iyengar, J. Tomasi, M. Cossi, N. Rega, J. M. Millam, M. Klene, J. E. Knox, J. B. Cross, V. Bakken, C. Adamo, J. Jaramillo, R. Gomperts, R. E. Stratmann, O. Yazyev, A. J. Austin, R. Cammi, C. Pomelli, J. W. Ochterski, R. L. Martin, K. Morokuma, V. G. Zakrzewski, G. A. Voth, P. Salvador, J. J. Dannenberg, S. Dapprich, A. D. Daniels, O. Farkas, J. B. Foresman, J. V. Ortiz,

J. Cioslowski and D. J. Fox, *Gaussian 09, Revision A.02*, Gaussian, Inc., Wallingford, CT, 2009.
50 B. O. Skadtchenko and R. Aroca, *Spectrochim. Acta, Part A*, 2001, **57**, 1009–1016.
51 H. Park, S. B. Lee, K. Kim and M. S. Kim, *J. Phys. Chem.*, 1990, **94**, 7576–7580.
52 R. Bauernschmitt and R. Ahlrichs, *Chem. Phys. Lett.*, 1996, **256**, 454–464.
53 N. Matsuda, K. Yoshii, K. Ataka, M. Osawa, T. Matsue and I. Uchida, *Chem. Lett.*, 1992, **21**, 1385–1388.
54 S. W. Han, I. Lee and K. Kim, *Langmuir*, 2002, **18**, 182–187.
55 M. Futamata, *J. Phys. Chem.*, 1995, **99**, 11901–11908.
56 K. Kim, Y. M. Lee, H. B. Lee, Y. Park, T. Y. Bae, Y. M. Jung, C. H. Choi and K. S. Shin, *J. Raman Spectrosc.*, 2010, **41**, 187–192.
57 M. Sun, Y. Hou, Z. Li, L. Liu and H. Xu, *Plasmonics*, 2011, **6**, 681–687.
58 K. S. Shin, H. S. Lee, S. W. Joo and K. Kim, *J. Phys. Chem. C*, 2007, **111**, 15223–15227.
59 L. B. Zhao, R. Huang, M. X. Bai, D. Y. Wu and Z. Q. Tian, *J. Phys. Chem. C*, 2011, **115**, 4174–4183.
60 W. H. Tsai, F. J. Boerio, S. J. Clarson and G. Montaudo, *J. Raman Spectrosc.*, 1990, **21**, 311–320.
61 B. Pergolese, M. Muniz-Miranda, G. Sbrana and A. Bigotto, *Faraday Discuss.*, 2006, **132**, 111–120.
62 M. Muniz-Miranda, B. Pergolese and A. Bigotto, *J. Phys. Chem. C*, 2008, **112**, 6988–6992.
63 B. Pergolese, M. Muniz-Miranda and A. Bigotto, *Chem. Phys. Lett.*, 2007, **438**, 290–293.
64 R. Holze, *Electrochim. Acta*, 1990, **35**, 1037–1044.
65 K. L. Posey, M. G. Viegas, A. J. Boucher, C. Wang, K. R. Stambaugh, M. M. Smith, B. G. Carpenter, B. L. Bridges, S. E. Baker and D. A. Perry, *J. Phys. Chem. C*, 2007, **111**, 12352–12360.
66 M. Xu, N. Lu, H. Xu, D. Qi, Y. Wang and L. Chi, *Langmuir*, 2009, **25**, 11216–11220.
67 N. J. Szabo and J. D. Winefordner, *Anal. Chem.*, 1997, **69**, 2418–2425.
68 A. S. L. Lee and Y.-S. Li, *J. Raman Spectrosc.*, 1994, **25**, 209–214.
69 Z. Wang, A. Bonoiu, M. Samoc, Y. Cui and P. N. Prasad, *Biosens. Bioelectron.*, 2008, **23**, 886–891.
70 D. Philip and G. Aruldhas, *J. Solid State Chem.*, 1995, **116**, 427–431.
71 K. Jackowska, J. Bukowska and A. Kudelski, *J. Electroanal. Chem.*, 1993, **350**, 177–187.
72 X. Dou, T. Takama, Y. Yamaguchi, H. Yamamoto and Y. Ozaki, *Anal. Chem.*, 1997, **69**, 1492–1495.
73 Y. C. Liu and R. L. McCreery, *Anal. Chem.*, 1997, **69**, 2091–2097.
74 P. Gao, D. Gosztola and M. J. Weaver, *J. Phys. Chem.*, 1988, **92**, 7122–7130.
75 C. Shi, W. Zhang, R. L. Birke, D. K. Gosser and J. R. Lombardi, *J. Phys. Chem.*, 1991, **95**, 6276–6285.
76 S. Schwamborn, L. Stoica, S. Neugebauer, T. Reda, H.-L. Schmidt and W. Schuhmann, *ChemPhysChem*, 2009, **10**, 1066–1070.
77 P. Gao, D. Gosztola and M. J. Weaver, *J. Phys. Chem.*, 1989, **93**, 3753–3760.
78 L. R. Sharma, A. K. Manchanda, G. Singh and R. S. Verma, *Electrochim. Acta*, 1982, **27**, 223–233.
79 W. A. Hayes and C. Shannon, *Langmuir*, 1996, **12**, 3688–3694.
80 J. Lukkari, K. Kleemola, M. Meretoja, T. Ollonqvist and J. Kankare, *Langmuir*, 1998, **14**, 1705–1715.
81 C. R. Raj, F. Kitamura and T. Ohsaka, *Langmuir*, 2001, **17**, 7378–7386.